VIII International Conference on Textile Composites and Inflatable Structures
STRUCTURAL MEMBRANES 2017
K.-U.Bletzinger, E. Oñate and B. Kröplin (Eds)

MEMBRANE ROOF STRUCTURES

CARSTEN CORTE

Baustatik – Baudynamik – Numerische Modellierung
Thrasoltstraße 12, D-10585 Berlin, Tel. / Fax +49-(0)30-347 871 78 / 80

Key words: elastic structural membranes, in-plane force equilibrium, static force equilibrium, dynamic force equilibrium, fluid-structure interaction, viscous fluid flow, membrane roof structures.

Summary. The governing equations for static structural membrane force equilibrium, for dynamic structural membrane force equilibrium and for transient strongly coupled fluid-structure interaction force equilibrium between structural membranes and viscous (laminar) fluids are presented. The approach for static and dynamic membrane force equilibrium is applied to a square Hypar membrane of 5 m edge length and ±0.0625 m vertical corner elevation. Furthermore, a steel cable net roof structure that spans over a museum building of 88 m × 52.8 m ground section is computationally represented by a membrane that satisfies stiffness as well as mass conservation in comparison with the steel cable net structure. To obtain sufficient curvature throughout the saddle shaped roof structure two Gaussian bell curves as well as two additional Hyparforms are considered for the overall shape of the cable net, i.e. the computational membrane. The roof structure is exposed to eigenload as well as to external load. Displacement results are shown for the different considered cases. To obtain a more detailed statement on external load due to surrounding flow viscous (laminar) fluid flow around the museum building and across its roof structure is computationally modeled. The procedure to interpolate fluid load onto the structural membrane and vice versa to interpolate structural membrane load onto the adjacent fluid is given.

1 INTRODUCTION

Frei [24], [25], [26], [27], [35] invented the membrane state of force equilibrium for the application of roof structures with comparitively small eigenmass per square meter of roof structure. Computational methods to model structural membranes force equilibrium were developed by Weitgespannte Flächentragwerke [38], [21], Zerning [42], Bubner [9], Weitgespannte Flächentragwerke [39], Bubner et al. [10], Brinkmann [7]. Reviews on structural membrane structures are given by Drew [22], [23], Hoppe [30], Berger [3], Schock [36], Renner [34], Apelmann et al. [1], Göppert [28], Cremers et al. [20], Seel et al. [37]. Neuhäuser et al. [33] show adaptive lightweight structures. Sophisticated numerical methods are developed by Trostel [26], Linkwitz et al. [32], Bufler [11], Bletzinger et al. [5], [6], [4], Wüchner et al. [40] with form finding of membrane structures by Wüchner [41], Linhard [31]. Corte et al. [12], [13] and Corte [14] show mutual force equilibrium based on weak [12] and strong [13], [14] coupling of fluid-structure interaction between elastic structures and viscous fluids. Corte [15], [16], [17] shows a consistent approach on fluid-structure interaction for large deformation with evaluation [15], [16] and application to a 3D elastic sail structure [17].

Corte [18], [19] shows a consistent computational approach for static and dynamic structural force equilibrium of elastic membrane structures.

As membrane roof structures generally possess curved shape it is difficult to define realistic dynamic load distribution due to surrounding fluid flow. The aim is to perform static membrane force equilibrium computations as well as dynamic membrane force equilibrium computations and to show the respective performance. With the next level of model complexity, surrounding viscous fluid flow around a considered structure is taken into account. Viscous fluid flow computations allow access to local fluid load onto the membrane roof structure and thus access to assessment of overall (transient) fluid load onto the considered membrane structure for design purpose.

2 COMPUTATIONAL APPROACH

2.1 Structural membrane force equilibrium

The computational model for the structural membrane approach applied here is explained in Corte [18], [19]. Along a spatial parameter coordinate system of ξ and η the undeformed stress-free shape of a considered membrane surface is defined by cartesian coordinates $[{}^0x(\xi,\eta),\ {}^0y(\xi,\eta),\ {}^0z(\xi,\eta)]$ together with its three-dimensional cartesian displacement $[{}^{t+\Delta t}u_{Sx}(\xi,\eta),\ {}^{t+\Delta t}u_{Sy}(\xi,\eta),\ {}^{t+\Delta t}u_{Sz}(\xi,\eta)]$ at a considered state $t+\Delta t$. The tensile force equilibrium within the membrane can be expressed with reference to the undeformed state 0 of the membrane (2^{nd} Piola-Kirchhoff stress, Green-Langrange strain) or with reference to the deformed stress-carrying state $t+\Delta t$ (Cauchy stress, Euler-Almansi strain), Bletzinger [4]; see Bathe [2] for detailed expressions on the definitions of the different stress and strain measures. The dynamic force equilibrium for structural membranes is here given in its form of virtual work expression as

$$\begin{aligned} &\int\int \quad [S_{\xi\xi}(\xi,\eta);\ S_{\eta\eta}(\xi,\eta);\ S_{\xi\eta}(\xi,\eta)]\bullet[\delta\varepsilon_{\xi\xi}(\xi,\eta);\ \delta\varepsilon_{\eta\eta}(\xi,\eta);\ \delta\varepsilon_{\xi\eta}(\xi,\eta)]^T\, dA(\xi,\eta)dx_{normal}(\xi,\eta) \\ &= \int\int \{\ \rho_S \cdot [\ddot{u}_{Sx}(\xi,\eta);\ \ddot{u}_{Sy}(\xi,\eta);\ \ddot{u}_{Sz}(\xi,\eta)]\bullet[\delta u_x(\xi,\eta);\ \delta u_y(\xi,\eta);\ \delta u_z(\xi,\eta)\ ]^T \\ &\quad + [f_{Sx}^{ext}(\xi,\eta);\ f_{Sy}^{ext}(\xi,\eta);\ f_{Sz}^{ext}(\xi,\eta)]\bullet[\delta u_x(\xi,\eta);\ \delta u_y(\xi,\eta);\ \delta u_z(\xi,\eta)\ ]^T\}dA(\xi,\eta)dx_{normal}(\xi,\eta) \end{aligned} \tag{1}$$

where nonlinear membrane stresses are defined as

$$\begin{aligned} &[S_{\xi\xi}(\xi,\eta); \quad [[C_{1111};\ C_{1122};\ C_{1112}]; \quad [\varepsilon_{\xi\xi}(\xi,\eta); \\ &S_{\eta\eta}(\xi,\eta); \ = \ [C_{2211};\ C_{2222};\ C_{2212}];\ \bullet \ \varepsilon_{\xi\eta}(\xi,\eta); \\ &S_{\xi\eta}(\xi,\eta)] \quad [C_{1211};\ C_{1222};\ C_{1212}]] \quad \varepsilon_{\eta\eta}(\xi,\eta)] \end{aligned} \tag{2}$$

with $[[C_{1111};\ C_{1122};\ C_{1112}];\ [C_{2211};\ C_{2222};\ C_{2212}];\ [C_{1211};\ C_{1222};\ C_{1212}]]$ constant elasticity tensor for linear elastic material and nonlinear strain defined as

$$\begin{aligned} &[\varepsilon_{\xi\xi}(\xi,\eta); \quad [[\partial u_\xi(\xi,\eta)/\partial x_\xi(\xi,\eta) + \tfrac{1}{2}\{\partial u_\xi(\xi,\eta)/\partial x_\xi(\xi,\eta)\}^2 + \tfrac{1}{2}\{\partial u_\eta(\xi,\eta)/\partial x_\xi(\xi,\eta)\}^2; \\ &\varepsilon_{\eta\eta}(\xi,\eta); \ = \ [\partial u_\eta(\xi,\eta)/\partial x_\eta(\xi,\eta) + \tfrac{1}{2}\{\partial u_\xi(\xi,\eta)/\partial x_\eta(\xi,\eta)\}^2 + \tfrac{1}{2}\{\partial u_\eta(\xi,\eta)/\partial x_\eta(\xi,\eta)\}^2; \\ &\varepsilon_{\xi\eta}(\xi,\eta)] \quad \{\ \partial u_\xi(\xi,\eta)/\partial x_\eta(\xi,\eta) + \partial u_\eta(\xi,\eta)/\partial x_\xi(\xi,\eta) \\ &\qquad + \partial u_\xi(\xi,\eta)/\partial x_\xi(\xi,\eta) + \partial u_\xi(\xi,\eta)/\partial x_\eta(\xi,\eta) \\ &\qquad + \partial u_\eta(\xi,\eta)/\partial x_\xi(\xi,\eta) + \partial u_\eta(\xi,\eta)/\partial x_\eta(\xi,\eta)\ \}] \end{aligned} \tag{3}$$

(ρ_S: structural density). Tangential vectors of the membrane surface along the spatial membrane parameter coordinates ξ and η are defined as ${}^0g_\xi(\xi,\eta)=\partial[{}^0x(\xi,\eta),\ {}^0y(\xi,\eta),\ {}^0z(\xi,\eta)]/\partial\xi$ and ${}^0g_\eta(\xi,\eta)=\partial[{}^0x(\xi,\eta),\ {}^0y(\xi,\eta),\ {}^0z(\xi,\eta)]/\partial\eta$ both with respect to the undeformed state 0 of the membrane or as ${}^{t+\Delta t}g_\xi(\xi,\eta)=\partial[{}^{t+\Delta t}x(\xi,\eta),\ {}^{t+\Delta t}y(\xi,\eta),\ {}^{t+\Delta t}z(\xi,\eta)]/\partial\xi$ and ${}^{t+\Delta t}g_\eta(\xi,\eta)=\partial[{}^{t+\Delta t}x(\xi,\eta),\ {}^{t+\Delta t}y(\xi,\eta),\ {}^{t+\Delta t}z(\xi,\eta)]/\partial\eta$ both with respect to the deformed state $t+\Delta t$ of the membrane. Appropriately the respective normal vector onto the membrane surface is defined as ${}^0g_{normal}(\xi,\eta)={}^0g_\xi(\xi,\eta)\times{}^0g_\eta(\xi,\eta)$ with respect to the undeformed state 0 of the membrane or as ${}^{t+\Delta t}g_{normal}(\xi,\eta)={}^{t+\Delta t}g_\xi(\xi,\eta)\times{}^{t+\Delta t}g_\eta(\xi,\eta)$ with respect to the deformed state $t+\Delta t$ of the membrane. With the above definitions displacement in local ξ and local η membrane direction is defined as ${}^{t+\Delta t}{}_0u_\xi(\xi,\eta)=[{}^{t+\Delta t}u_{Sx}(\xi,\eta),\ {}^{t+\Delta t}u_{Sy}(\xi,\eta),\ {}^{t+\Delta t}u_{Sz}(\xi,\eta)]\bullet{}^0g_\xi(\xi,\eta)$ and ${}^{t+\Delta t}{}_0u_\eta(\xi,\eta)=[{}^{t+\Delta t}u_{Sx}(\xi,\eta),\ {}^{t+\Delta t}u_{Sy}(\xi,\eta),\ {}^{t+\Delta t}u_{Sz}(\xi,\eta)]\bullet{}^0g_\eta(\xi,\eta)$ with respect to the undeformed state 0 as well as ${}^{t+\Delta t}{}_{t+\Delta t}u_\xi(\xi,\eta)=[{}^{t+\Delta t}u_{Sx}(\xi,\eta),\ {}^{t+\Delta t}u_{Sy}(\xi,\eta),\ {}^{t+\Delta t}u_{Sz}(\xi,\eta)]\bullet{}^{t+\Delta t}g_\xi(\xi,\eta)$ and ${}^{t+\Delta t}{}_{t+\Delta t}u_\eta(\xi,\eta)=[{}^{t+\Delta t}u_{Sx}(\xi,\eta),\ {}^{t+\Delta t}u_{Sy}(\xi,\eta),\ {}^{t+\Delta t}u_{Sz}(\xi,\eta)]\bullet{}^{t+\Delta t}g_\eta(\xi,\eta)$ with respect to the deformed state $t+\Delta t$, respectively. Within equation (1) the *virtual* strain expressions are assumed to be the linear part of strain defined in equation (3); so equation (1) becomes unique in unknowns $[{}^{t+\Delta t}u_{Sx}(\xi,\eta),\ {}^{t+\Delta t}u_{Sy}(\xi,\eta),\ {}^{t+\Delta t}u_{Sz}(\xi,\eta)]$ at a considered state $t+\Delta t$. The analytic expression for the membrane area differetial is $d^0A(\xi,\eta)={}^0g_\xi(\xi,\eta)\times{}^0g_\eta(\xi,\eta)d\xi d\eta$ and $d^{t+\Delta t}A(\xi,\eta)={}^{t+\Delta t}g_\xi(\xi,\eta)\times{}^{t+\Delta t}g_\eta(\xi,\eta)d\xi d\eta$, respectively. ${}^0x_{normal}(\xi,\eta)$ and ${}^{t+\Delta t}x_{normal}(\xi,\eta)$, respectively, is membrane thickness at state 0 and state $t+\Delta t$, respectively.

Equation (1) describes the general dynamic membrane force equilibrium. In case the mass (inertia) term $\int\int \rho_S \cdot [\ddot{u}_{Sx}(\xi,\eta);\ \ddot{u}_{Sy}(\xi,\eta);\ \ddot{u}_{Sz}(\xi,\eta)]\bullet[\delta u_x\ (\xi,\eta);\ \delta u_y\ (\xi,\eta);\ \delta u_z\ (\xi,\eta)\ ]^T\ dA(\xi,\eta)x_{normal}(\xi,\eta)$ in equation (1) is neglected then the general static membrane force equilibrium is described. For the applied finite element approach the considered continuous membrane domain is spatially discretized by discrete 3D nodes with nodal 3D displacement $[u_{Sx},\ u_{Sy},\ u_{Sz}]$ and by 9-node-4-corner finite elements with interpolation functions that have quadratic polynomials in ξ and quadratic polynomials in η, Corte [18], [19]. In time direction discretization is performed by the HHT-α method (Hilber et al. [29]), Corte [18], [19].

2.2 Viscous laminar fluid force equilibrium and fluid incompressibity

To obtain access to action of the surrounding flow around the considered structure and in particular across the considered membrane roof structure (here laminar) viscous fluid flow is described by the incompressible Navier-Stokes equation that is expressed as

$$\begin{aligned}&[\rho_F\partial u_x/\partial t+\rho_F u_x\,\partial u_x/\partial x+\rho_F u_y\,\partial u_x/\partial y+\rho_F u_z\,\partial u_x/\partial z-\mu_F(\partial^2u_x/\partial x^2+\partial^2u_x/\partial y^2+\partial^2u_x/\partial z^2)+\partial p_F/\partial x;\ [f_{Fx}{}^{ext};\\ &\rho_F\partial u_y/\partial t+\rho_F u_x\,\partial u_y/\partial x+\rho_F u_y\,\partial u_y/\partial y+\rho_F u_z\,\partial u_y/\partial z-\mu_F(\partial^2u_y/\partial x^2+\partial^2u_y/\partial y^2+\partial^2u_y/\partial z^2)+\partial p_F/\partial y;=f_{Fy}{}^{ext};\\ &\rho_F\partial u_z/\partial t+\rho_F u_x\,\partial u_z/\partial x+\rho_F u_y\,\partial u_z/\partial y+\rho_F u_z\,\partial u_z/\partial z-\mu_F(\partial^2u_z/\partial x^2+\partial^2u_z/\partial y^2+\partial^2u_z/\partial z^2)+\partial p_F/\ \partial z]\ \ f_{Fz}{}^{ext}]\end{aligned} \tag{4}$$

with the incompressibility demand

$$\partial u_x/\partial x+\partial u_y/\partial y+\partial u_x/\partial z = 0 \tag{5}$$

($[u_x, u_y, u_z]$: fluid velocity, ρ_F: fluid density, μ_F: fluid (dynamic) viscosity).

Equations (4) and (5) are both discretized in space direction with discrete 3D fluid node and $[u_x, u_y, u_z, p_F]$ as nodal unknowns fluid velocity cartesian components and fluid pressure and 8-node hexahedra elements with linear interpolation functions in each elementwise local coordinate ξ, η and ζ direction. In equation (4) for time discretization the Euler backwards (one-step) method is applied. For consideration of the flow direction that becomes of importance in the convective terms of equation (4) appropriate artificial diffusion is introduced within the convective terms of equation (4). The artificial diffusion is considered componentwise in x-, in y- and in z-direction following the componentwise 1D analytic expression $[u_x h_x/2 \cdot \coth(u_x h_x/(2\mu_F)); u_y h_y/2 \cdot \coth(u_y h_y/(2\mu_F)); u_z h_z/2 \cdot \coth(u_z h_z/(2\mu_F))]$, h_x: max $|x_i - x_j|$, h_y: max $|y_i - y_j|$, h_z: max $|z_i - z_j|$, $i \neq j$, i, j=1...8: element´s local nodes´ indices, that is shown in Brooks and Hughes [8]. Equation (4) is solved componentwise for fluid velocity components $[u_x, u_y, u_z]$ at the new timestep of a considered discrete time interval, assuming an up-to-then known pressure distribution within the fluid domain. With the incompressibility demand in equation (5) that is inserted into equation (4) the resulting equation [(5) in (4)] is then solved for the pressure at the new timestep of the considered discrete time interval, using the already-computed fluid velocity field $[u_x, u_y, u_z]$ that was obtained from solving equation (4). By computing the pressure at the new timestep from equation [(5) in (4)] the before-assumed pressure distribution for solving equation (4) is corrected in that particular way that the computed-by-equation (4) fluid velocity for the new timestep is incompressible regarding the computed-by-equation [(5) in (4)] pressure distribution at the new timestep. Within a considered discrete time interval there are iterations performed on the sequence of solving equation (4) for the fluid velocity at the new timestep and then solving equation [(5) in (4)] for the fluid pressure at the new timestep. It is remarked here that by using equation [(5) in (4)] to obtain the appropriate fluid pressure distribution at the new timestep the full incompressibility demand is kept. No weakening of the incompressibility demand equation (5) is introduced into the computational approach during discretization.

2.3 Fluid-structure interaction between elastic structural membrane and viscous laminar fluid with fluid incompressibility

The fluid-structure interaction between elastic structural membranes and viscous (here laminar) fluids with fluid incompressibility is achieved by strong segregated coupling of fluid forces onto the structure and structural forces onto the fluid across the common fluid-structure interface that both elastic membrane structure and viscous fluid share with each other. In the application that is treated here the common fluid-structure interface consists of the considered structural membrane and the fluid boundary that is adjacent to the structural membrane. Due to the curved shape of the respective structural membrane and due to the wide-range fluid environment around the considered structure for the membrane spatial finite element discretization and the fluid domain spatial finite element discretization on the fluid-structure interface two different non-matching node distributions are used for the structural membrane on the one hand side and the fluid domain on the other hand side.
The equation that describes the dynamic structural membrane force equilibrium is extended to consider fluid load in addition to other external load onto the structure, i.e. equation (1) is extended to

$$\int\int [S_{\xi\xi}(\xi,\eta); S_{\eta\eta}(\xi,\eta); S_{\xi\eta}(\xi,\eta)]\bullet[\delta\varepsilon_{\xi\xi}(\xi,\eta); \delta\varepsilon_{\eta\eta}(\xi,\eta); \delta\varepsilon_{\xi\eta}(\xi,\eta)]^T dA(\xi,\eta)dx_{normal}(\xi,\eta)$$
$$= \int\int \{\rho_S \cdot [\ddot{u}_{Sx}(\xi,\eta); \ddot{u}_{Sy}(\xi,\eta); \ddot{u}_{Sz}(\xi,\eta)]\bullet[\delta u_x(\xi,\eta); \delta u_y(\xi,\eta); \delta u_z(\xi,\eta)]^T \quad (6)$$
$$+[f_{Sx}^{ext}(\xi,\eta); f_{Sy}^{ext}(\xi,\eta); f_{Sz}^{ext}(\xi,\eta)]\bullet[\delta u_x(\xi,\eta); \delta u_y(\xi,\eta); \delta u_z(\xi,\eta)]^T\} dA(\xi,\eta)dx_{normal}(\xi,\eta)$$
$$-\{\int\int\int$$
$$[\rho_F\partial u_x/\partial t+\rho_F u_x\partial u_x/\partial x+\rho_F u_y\partial u_x/\partial y+\rho_F u_z\partial u_x/\partial z-\mu_F(\partial^2 u_x/\partial x^2+\partial^2 u_x/\partial y^2+\partial^2 u_x/\partial z^2)+\partial p_F/\partial x;\ [w_x;$$
$$\rho_F\partial u_y/\partial t+\rho_F u_x\partial u_y/\partial x+\rho_F u_y\partial u_y/\partial y+\rho_F u_z\partial u_y/\partial z-\mu_F(\partial^2 u_y/\partial x^2+\partial^2 u_y/\partial y^2+\partial^2 u_y/\partial z^2)+\partial p_F/\partial y;\bullet w_y;$$
$$\rho_F\partial u_z/\partial t+\rho_F u_x\partial u_z/\partial x+\rho_F u_y\partial u_z/\partial y+\rho_F u_z\partial u_z/\partial z-\mu_F(\partial^2 u_z/\partial x^2+\partial^2 u_z/\partial y^2+\partial^2 u_z/\partial z^2)+\partial p_F/\partial z]\ \ w_z]$$
$$-[f_{Fx}^{ext};\ [w_x;$$
$$f_{Fy}^{ext};\bullet w_y;$$
$$f_{Fz}^{ext}]\ w_z]$$
$$\} dx(\xi,\eta,\zeta)\, dy(\xi,\eta,\zeta)\, dz(\xi,\eta,\zeta)$$

on the shared common fluid-structure interface (w_x, w_y, w_z: weighing functions for x-, y- and z-fluid forces).

On the other hand the equation that describes the fluid force equilibrium is extended to consider structural load in addition to other external load onto the fluid, i.e. equation (4) is extended to (weighed weak integral form here)

$$\{\int\int\int$$
$$[\rho_F\partial u_x/\partial t+\rho_F u_x\partial u_x/\partial x+\rho_F u_y\partial u_x/\partial y+\rho_F u_z\partial u_x/\partial z-\mu_F(\partial^2 u_x/\partial x^2+\partial^2 u_x/\partial y^2+\partial^2 u_x/\partial z^2)+\partial p_F/\partial x;\ [w_x;$$
$$\rho_F\partial u_y/\partial t+\rho_F u_x\partial u_y/\partial x+\rho_F u_y\partial u_y/\partial y+\rho_F u_z\partial u_y/\partial z-\mu_F(\partial^2 u_y/\partial x^2+\partial^2 u_y/\partial y^2+\partial^2 u_y/\partial z^2)+\partial p_F/\partial y;\bullet w_y;$$
$$\rho_F\partial u_z/\partial t+\rho_F u_x\partial u_z/\partial x+\rho_F u_y\partial u_z/\partial y+\rho_F u_z\partial u_z/\partial z-\mu_F(\partial^2 u_z/\partial x^2+\partial^2 u_z/\partial y^2+\partial^2 u_z/\partial z^2)+\partial p_F/\partial z]\ \ w_z]$$
$$-[f_{Fx}^{ext};\ [w_x;$$
$$f_{Fy}^{ext};\bullet w_y;$$
$$f_{Fz}^{ext}]\ w_z]$$
$$\} dx(\xi,\eta,\zeta)\, dy(\xi,\eta,\zeta)\, dz(\xi,\eta,\zeta)$$
$$-\{ \quad (7)$$
$$\int\int [S_{\xi\xi}(\xi,\eta); S_{\eta\eta}(\xi,\eta); S_{\xi\eta}(\xi,\eta)]\bullet[\delta\varepsilon_{\xi\xi}(\xi,\eta); \delta\varepsilon_{\eta\eta}(\xi,\eta); \delta\varepsilon_{\xi\eta}(\xi,\eta)]^T\ dA(\xi,\eta)dx_{normal}(\xi,\eta)$$
$$-\int\int \{\rho_S \cdot [\ddot{u}_{Sx}(\xi,\eta); \ddot{u}_{Sy}(\xi,\eta); \ddot{u}_{Sz}(\xi,\eta)]\bullet[\delta u_x(\xi,\eta); \delta u_y(\xi,\eta); \delta u_z(\xi,\eta)]^T$$
$$+ [f_{Sx}^{ext}(\xi,\eta); f_{Sy}^{ext}(\xi,\eta); f_{Sz}^{ext}(\xi,\eta)]\bullet[\delta u_x(\xi,\eta); \delta u_y(\xi,\eta); \delta u_z(\xi,\eta)]^T\ \} dA(\xi,\eta)dx_{normal}(\xi,\eta)$$
$$\} = [0;0;0]^T$$

on the shared common fluid-structure interface, where the fluid incompressibility demand equation (5) in its analytic form stays the same, i.e. stays

$$\partial u_x/\partial x+\partial u_y/\partial y+\partial u_x/\partial z = 0 \quad (8)$$

on the shared common fluid-structure interface.

Because of – as mentioned above – the non-matching two different meshes for the structural side and the fluid side an interpolation procedure becomes necessary to interpolate fluid force data onto positions of structural nodes and vice versa to interpolate structural force data onto positions of fluid nodes. The two directions (fluid → structure; structure → fluid) of interpolation procedure involve determination of intrinsic local coordinates ξ and η and thus solving (nonlinear) equation systems for the purpose of exact load transfer from the fluid onto the structure and from the structure onto the fluid. The solution to obtain exact intrinsic local coordinates ξ and η is satisfied by the two interpolation procedures

Find (ξ_F, η_F):

$$\{F_F(\xi_F, \eta_F) = | [p_x^{Structure}; p_y^{Structure}; p_z^{Structure}] - \Sigma_{i=1...4}[p_{i,x}^{Fluid}; p_{i,y}^{Fluid}; p_{i,z}^{Fluid}] \cdot N_i^{Fluid}(\xi_F, \eta_F) | = minimum\} \wedge \{\xi_F \in [-1;1]\} \wedge \{\eta_F \in [-1;1]\}.$$

($[p_x^{Structure}; p_y^{Structure}; p_z^{Structure}]$: considered structural node, $[p_{i,x}^{Fluid}; p_{i,y}^{Fluid}; p_{i,z}^{Fluid}]$, i=1...4: fluid element´s surface nodes, $N_i^{Fluid}(\xi_F, \eta_F)$, i=1...4: bilinear fluid nodes´ interpolation functions on appropriate fluid element´s surface) for to interpolate fluid force data onto the considered structural mesh node and

Find (ξ_S, η_S):

$$\{F_S(\xi_S, \eta_S) = | [p_x^{Fluid}; p_y^{Fluid}; p_z^{Fluid}] - \Sigma_{i=1...9}[p_{i,x}^{Structure}; p_{i,y}^{Structure}; p_{i,z}^{Structure}] \cdot N_i^{Structure}(\xi_S, \eta_S) | = minimum\} \wedge \{\xi_S \in [-1;1]\} \wedge \{\eta_S \in [-1;1]\}.$$

($[p_x^{Fluid}; p_y^{Fluid}; p_z^{Fluid}]$: considered fluid node, $[p_{i,x}^{Structure}; p_{i,y}^{Structure}; p_{i,z}^{Structure}]$, i=1...9: structural element´s nodes, $N_i^{Structure}(\xi_S, \eta_S)$, i=1...9: binonlinear structural nodes´ interpolation functions) for to interpolate structural force data onto the considered fluid mesh node. The interpolation procedure of fluid force data onto the structural mesh is linear in (ξ_F, η_F) (8-node hexahedra fluid elements, linear interpolation functions) whereas the interpolation procedure of structural data onto the fluid mesh is nonlinear in (ξ_S, η_S) (9-node-4-corner structural membrane elements, quadratic interpolation functions, Corte [18], [19]). $\partial F_F(\xi_F, \eta_F)/\partial\xi_F = 0$ and $\partial F_F(\xi_F, \eta_F)/\partial\eta_F = 0$ appropriately deliver (ξ_F, η_F), $\partial F_S(\xi_S, \eta_S)/\partial\xi_S = 0$ and $\partial F_S(\xi_S, \eta_S)/\partial\eta_S = 0$ appropriately deliver (ξ_S, η_S).

3 HYPARFORM (L=5 M)

A membrane with initial stress-free (displacement and strain equal zero) Hypar shape of 5 m edge length (ground view) and ±0.0625 m vertical corner elevation is considered. The membrane is discretized with 15×15=225 nodes and 7×7=49 9-node-4-corner finite elements of quadratic interpolation functions.

3.1 Hyparform (L=5 m): Static force equilibrium

The membrane has material properties modulus of elasticity E=2.5e7 N/m², Poisson´s ratio ν=0.25, density ρ=1000 kg/m³ and membrane thickness of 0.001 m. Gravity is assumed with 10 m/s². The membrane is exposed to 100 times of its eigenload, i.e. to 100·10 m/s²·1000 kg/m³·0.001 m = 1000 N/m² in (vertical) gravity direction. Boundary conditions define completely fixed displacement (ux=0, uy=0, uz=0) on the four edges of the membrane. In the inner part of the membrane surface, excluding the four boundary edges, case i) horizontal displacement is fixed (ux=0, uy=0) and vertical displacement is free (uz: free), case ii) horizontal displacement is free (ux: free, uy: free) and vertical displacement is free (uz: free). For case i) 200 equilibrium iterations, for case ii) 10000 equilibrium iterations are performed. For both case i) and ii) the size of the displacement increment within an equilibrium iteration is limited to 0.01 m as the maximum for one single displacement component (ux, uy or uz) of one single node within the all-nodes-covering displacement increment vector. For case i) a

strictly monotonic increase of the vertical displacement at the membrane center (uz of node 201, degree of freedom 603) appears that reaches a value of uz=0.16 m after 200 equilibrium iterations. For case ii) a vertical displacement at the membrane center (uz of node 201, degree of freedom 603) reaches 0.25 m after less than 1000 equilibrium iterations and then stays around 0.25 m for until 10000 equilibrium iterations. The iterative solutions for case i) and ii) and the appropriate membrane undisplaced and displaced shape for case i) and ii) are shown in figure 1.

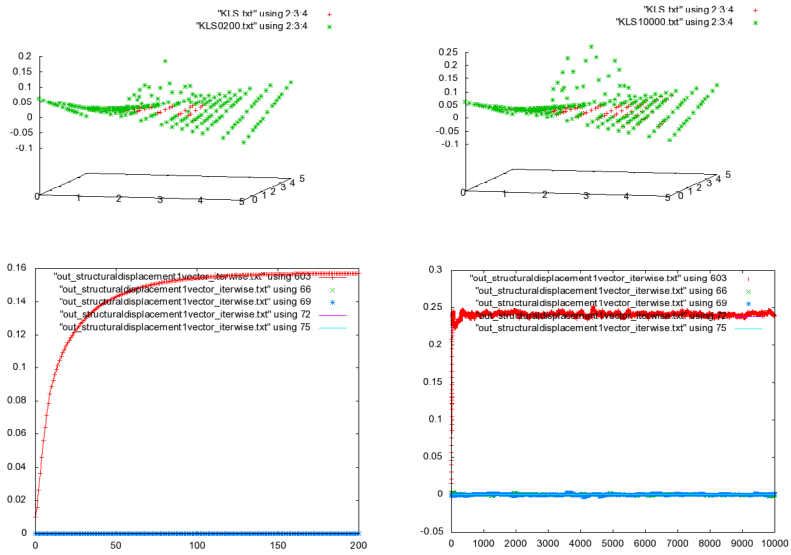

Figure 1: square Hypar membrane (L=5 m), ±0.0625 m vertical corner elevation: undeformed and deformed membrane shape (top row) [in m] and membrane center vertical displacement [in m] over cumulated equilibrium iteration index (bottom row) for case i) field displacement [ux=0, uy=0, uz: free] within the inner part of the membrane (left column) and for case ii) field displacement [ux: free, uy: free, uz: free] within the inner part of the membrane (right column) (vertical displacement in load direction is plotted upward here (in this figure))

3.2 Hyparform (L=5 m): Dynamic force equilibrium

For the three cases iii), iv) and v) transient external load is applied to the membrane in time domain.

For case iii) membrane material properties are E=2.5e7 N/m², ν=0.25, ρ=1000 kg/m³ and membrane thickness is 0.001 m. Transient harmonic external load ranges from 100 times to 300 times of its eigenload and follows the time-t-dependent function $[2+\cos(2\pi\cdot 0.1\text{Hz}\cdot t)]\cdot 100\cdot 10$ m/s²·1000 kg/m³·0.001 m = $[2+\cos(2\pi\cdot 0.1\text{Hz}\cdot t)]\cdot 1000$ N/m² in (vertical) gravity direction with 0.1 Hz oscillation frequency. Time integration is performed for 20 time intervals of 0.5 s constant time interval size with 10 s total time. Within each considered time interval 1000 equilibrium iterations are performed. The HHT-α parameter is selected as α_{HHT}=-0.1. The size of the displacement increment is limited to 0.01 m as the maximum for one single displacement component (ux, uy or uz) of one single node within the all-nodes-covering displacement increment vector.

For case iv) and v) membrane material properties E, ν and ρ are selected to represent a cable-net structure that consists of crosswise orthogonal steel cables of 5 mm=0.005 m diameter (cross-section area $\pi\cdot(0.0025\ \text{m})^2\approx 0.00002\ \text{m}^2$) of 0.357 m distance from each other. For steel it is set E_{Steel}=2.1e11 N/m², ν_{Steel}=0.3, ρ_{Steel}=7860 kg/m³. So for one square meter of the membrane the membrane mass shall represent one square meter of the steel cable net, and for one meter width of the membrane the membrane stiffness shall represent one meter width of the steel cable net. The computational membrane material parameters E, ν and ρ and the membrane thickness d are derived as follows (A in m²/(width in m), A_{Steel} in m²/(width in m)):

$EA=E\cdot 1\ \text{m}\cdot d/(1\ \text{m})=E_{Steel}\,A_{steel}$
$\nu=\nu_{Steel}$
$\rho_{Steel}(A_{Steel}\cdot 1\ \text{m})\cdot 1\ \text{m}+\rho_{Steel}(A_{Steel}\cdot 1\ \text{m})\cdot 1\ \text{m}=\rho\cdot 1\ \text{m}\cdot 1\ \text{m}\cdot d$
(longitudinal) (orthogonal) (1 m² membrane)

$EA=E\cdot 1\ \text{m}\cdot d/(1\ \text{m})=E_{Steel}\,A_{steel}$
The computational membrane thickness d is selected here as d=1 mm=0.001 m.
$EA=E\cdot 1\ \text{m}\cdot 0.001\ \text{m}/(1\ \text{m})\approx 2.1\text{e}11\ \text{N/m}^2\cdot 0.00002\ \text{m}^2/(0.357\ \text{m})$
$\underline{E}\approx[2.1\text{e}11\ \text{N/m}^2\cdot 0.00002\ \text{m}^2/(0.357\ \text{m})]/[1\ \text{m}\cdot 0.001\ \text{m}/(1\ \text{m})]\approx\underline{1.175\text{e}10\ \text{N/m}^2}$
$\underline{\nu}=\nu_{Steel}=\underline{0.3}$
$\rho\approx[7860\ \text{kg/m}^3\cdot(0.00002\ \text{m}^2/(0.357\ \text{m})\cdot 1\ \text{m})\cdot 1\ \text{m}$
$+7860\ \text{kg/m}^3\cdot(0.00002\ \text{m}^2/(0.357\ \text{m})\cdot 1\ \text{m})\cdot 1\ \text{m}]/[1\ \text{m}\cdot 1\ \text{m}\cdot d]$
$\underline{\rho}\approx 2\cdot[7860\ \text{kg/m}^3\cdot 0.00002\ \text{m}^2/(0.357\ \text{m})\cdot 1\ \text{m}^2]/[1\ \text{m}^2\cdot 0.001\ \text{m}]\approx\underline{880\ \text{kg/m}^3}$

As a simplification it is assumed here that for case iv) and v) the steel cable net is computationally represented by a membrane that has isotropic material properties (E, ν). For cases iii), iv) and v) boundary conditions define completely fixed displacement (ux=0, uy=0, uz=0) on the four edges of the membrane, whereas in the inner part of the membrane surface, excluding the four boundary edges, horizontal displacement is free (ux: free, uy: free) and vertical displacement is free (uz: free). Time integration is performed, case iii) and iv), for 20 time intervals of constant time interval size 0.5 s, 10 s total time, case v) for 235 time intervals of 0.1 s constant time interval size, 23.5 s total time. Within each considered time interval for case iii) 100 equilibrium iterations, for case iv) and v) 1000 equilibrium iterations are performed. The HHT-α parameter is selected as α_{HHT}=-0.1. The size of the displacement increment is limited to 0.01 m for case iii) and limited to 0.0001 m for case iv) and v) as the maximum for one single displacement component (ux, uy or uz) of one single node within the all-nodes-covering displacement increment vector. Figure 2 shows the transient evolution of the vertical displacement of the membrane center (uz of node 201, degree of freedom 603) and the undeformed and timestep-selected deformed shape of the membrane for cases iii), iv) and v). For material properties E=2.5e7 N/m², ρ=1000 kg/m³, case iii), vertical displacement of the membrane center ranges between 0.25 m and 0.30 m, for material properties E≈1.175e10 N/m², ρ≈880 kg/m³, case iv) and v), vertical displacement of the membrane center ranges between 0.04 m and 0.06 m.

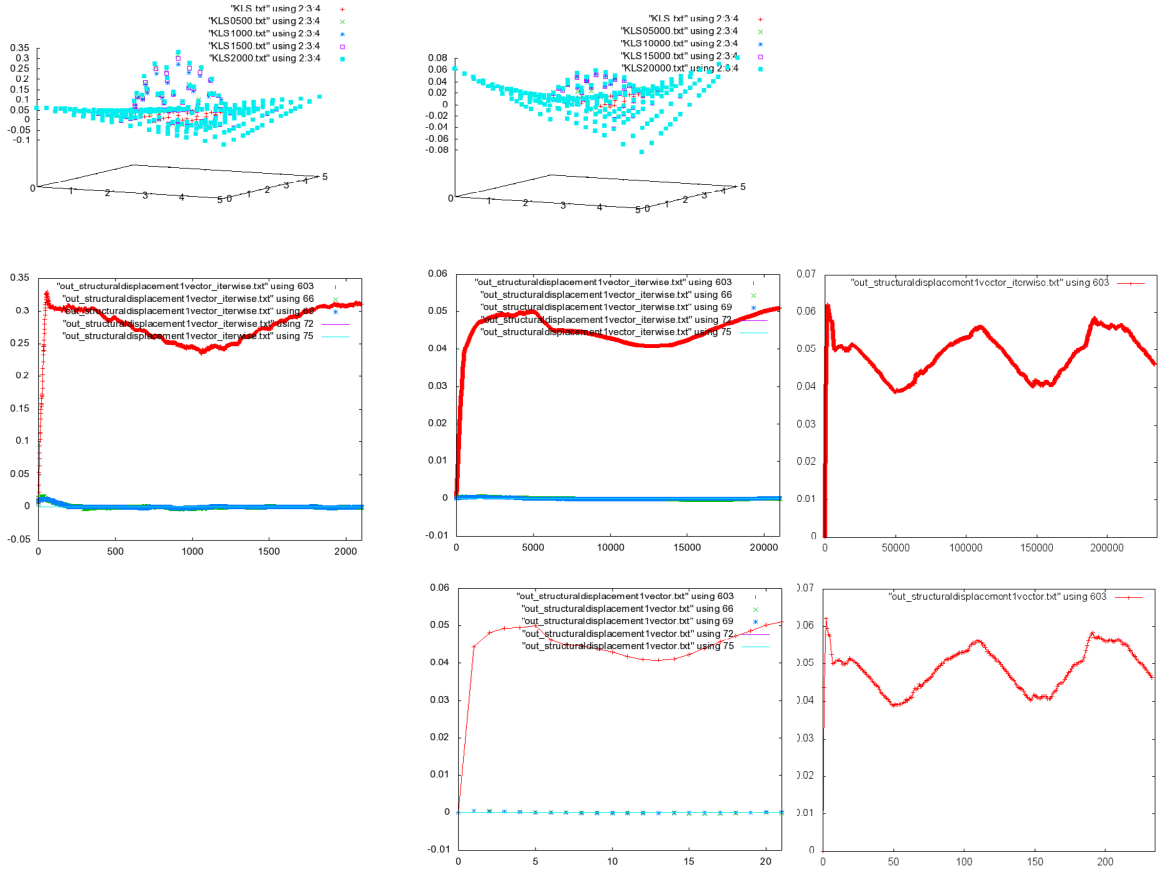

Figure 2: square Hypar membrane (L=5 m), ±0.0625 m vertical corner elevation: undeformed and deformed membrane shape (top row) [in m] and membrane center vertical displacement [in m] over cumulated equilibrium iteration index (center row) and over timestep index (bottom row) for case iii) Δt=0.5 s, 100 equilibrium iterations per time interval (left column), case iv) Δt=0.5 s, 1000 equilibrium iterations per time interval (center column), case v) Δt=0.1 s, 1000 equilibrium iterations per time interval (right column); case iii), iv) and v) field displacement [ux: free, uy: free, uz: free] within the inner part of the membrane (vertical displacement in load direction is plotted upward here (in this figure))

4 ROOF STRUCTURE (L=88 M, B=52.8 M)

A saddle-shaped roof structure of 88 m × 52.8 m ground section for a museum building of 13 m height above ground in the design process shall be analyzed. The ground view horizontal coordinates for the roof reach from (x=0, y=0) to (x=88 m, y=52.8 m). The museum of lower level, base level and first floor carries a steel cable net roof (→ computationally represented by an elastic membrane roof) above with central roof ridge of 5.28 m relative height at horizontal coordinate y=26.4 m. The roof consists of crosswise orthogonal steel cables of 20 mm=0.02 m diameter (cross-section area π·(0.01

m)²≈0.00031415 m²) of 0.50 m distance from each other. The steel cable net is represented by an elastic membrane with isotropic material properties that consider mass conservation as well as stiffness conservation from the steel cable net geometry to the computational elastic membrane. The membrane roof is supported along the circumventing (here rigid) beam structure at the gutter, along the roof ridge, along four intermediate girders from gutter to roof ridge and along the zero-curvature-rings of two radial Gaussian bell curve shaped roof shapes, each of which is located individually on each of the two sides of the roof ridge and one of which has a maximum vertical elevation of 5.28 m and the other one of which has a maximum vertical elevation of 3.28 m each at their respective radial center. During the design process, the curvature of the membrane shape is analyzed analytically, and as static displacement computations show large displacement where Gaussian bell curve curvature becomes very small, two Hypar shapes of ±1.20 m vertical corner elevation and two Hypar shapes of ±0.35 m vertical corner elevation, respectively, are added to increase the membrane system stiffness where Gaussian bell curve curvature becomes very small. The eventually found final Gaussian bell curve and Hypar shaped membrane roof is exposed to static external load (10 times of its eigenload; 1 time of its eigenload). In a more complex model, the geometry of the museum building is surrounded by viscous fluid flow, and fluid-structure interaction (FSI) is intended between the elastic membrane roof structure and the adjacent viscous fluid flow in time domain. The fluid-structure interaction approach is based on the mutual force equilibrium of viscous fluid forces and elastic structural forces on the shared common geometric fluid-structure interface. The membrane roof of 88 m × 52.8 m ground section is discretized by 33×29=957 nodes and 16×14=224 9-node-4-corner finite elements. The geometric distribution of the finite element nodes that represent the membrane roof shape is illustrated in figure 3.

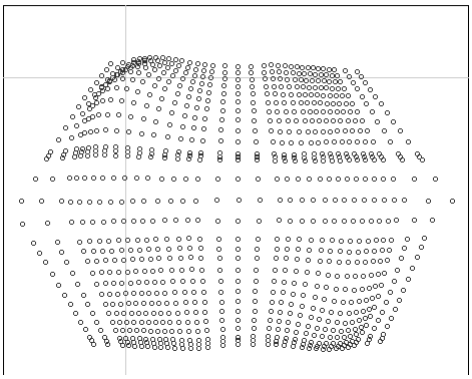

Figure 3: topview onto structural membrane nodes: Gaussian bell curves and Hypar ±0.35 m (x here from left to right, y here (in this plot) from top to bottom (!))

The shape of the membrane roof is given here more in detail. For structural computations the membrane roof structure is rigidly fixed in all three cartesian components of nodal displacement at planes x=0, x=35 m, x=53 m, x=88 m, y=0, y=26.4 m, y=52.8 m and at the two (x,y)-curves for which the curvature of the two Gaussian bell curves is zero. The two Gaussian bell curves have their respective radial centers at (x_A, y_A)=(17 m, 12 m) (Gaussian bell curve height z_A=5.28 m at (x_A, y_A) with raduis R_A=8 m and at (x_B, y_B)=(71 m, 42.8 m)

(Gaussian bell curve height z_B=3.28 m at (x_B, y_B) with radius R_B=8 m. Radius R_A and R_B label the radial distance from the radial center of the Gaussian bell curve to where the curvature of the Gaussian bell curve is zero. Each of the two Gaussian bell curves holds on one of the two sides of the roof ridge. The two Gaussian bell curves follow the function

$$z(x,y) = z_m \cdot e^{-\lambda^2[(x-xm)^2+(y-ym)^2]} = z(r(x,y)) = z_m \cdot e^{-\lambda^2[r(x,y)^2]}$$

where $r(x,y)=\mathrm{sqrt}[(x-x_m)^2+(y-y_m)^2]$, $z_m=z_A$, $x_m=x_A$, $y_m=y_A$ and $z_m=z_B$, $x_m=x_B$, $y_m=y_B$ for the two different Gaussian bell curves. First radial derivative (radial slope) and second radial derivative (approximation for radial curvature) of the Gaussian bell curves are

$$\partial z(x,y)/\partial r(x,y) = -2 \cdot r(x,y) \cdot \lambda^2 \cdot z_m \cdot e^{-\lambda^2[r(x,y)^2]},$$
$$\partial^2 z(x,y)/\partial[r(x,y)]^2 = (-2+4\cdot[r(x,y)]^2\cdot\lambda^2)\cdot\lambda^2\cdot z_m \cdot e^{-\lambda^2[r(x,y)^2]}$$

. Demanding for the approximation of the curvature that $\partial^2 z(x,y)/\partial[r(x,y)]^2=0$ it follows

$$r(x,y) = 1/[\mathrm{sqrt}[2] \cdot \lambda] \text{ at } \partial^2 z(x,y)/\partial[r(x,y)]^2=0,$$
$$\lambda = 1/[\mathrm{sqrt}[2] \cdot r(x,y)] \text{ at } \partial^2 z(x,y)/\partial[r(x,y)]^2=0.$$

The radial distance where the Gaussian bells curves shall have zero curvature is here selected to be $r(x,y)=R_m=R_A$ and $r(x,y)=R_m=R_B$, respectively. The appropriate value of λ follows as (here $R_m=R_A$= 8 m, $R_m=R_B$= 8 m)

$$\lambda = 1/[\mathrm{sqrt}[2] \cdot 8\ \mathrm{m}] \approx 0.088388\ 1/\mathrm{m} \text{ for } \partial^2 z(x,y)/\partial[r(x,y)]^2=0 \text{ at } r(x,y)=R_m$$

. For the selected values $R_m=R_A$=8 m and $R_m=R_B$=8 m the height ($R_m=R_A$=8 m, z_A=5.28 m), the slope and the (approximation of) curvature are computed ($0\cdot R_m$=0, $1\cdot R_m$=8 m, $2\cdot R_m$=16 m, $3\cdot R_m$=24 m) as

[z(x,y)](r(x,y)=0·R_m) = 5.28 m (for $R_m=R_A$=8 m, z_A=5.28 m)
[z(x,y)](r(x,y)=1·R_m) ≈ 3.20 m (for $R_m=R_A$=8 m, z_A=5.28 m)
[z(x,y)](r(x,y)=2·R_m) ≈ 0.71 m (for $R_m=R_A$=8 m, z_A=5.28 m)
[z(x,y)](r(x,y)=3·R_m) ≈ 0.058 m (for $R_m=R_A$=8 m, z_A=5.28 m)

[∂ z(x,y)/∂ r(x,y)](r(x,y)=0·R_m) = 0 m/m (slope 0° , $R_m=R_A$=8 m, z_A=5.28 m)
[∂ z(x,y)/∂ r(x,y)](r(x,y)=1·R_m) ≈ -0.40030 m/m (slope -21.81°, $R_m=R_A$=8 m, z_A=5.28 m)
[∂ z(x,y)/∂ r(x,y)](r(x,y)=2·R_m) ≈ -0.17864 m/m (slope -10.12°, $R_m=R_A$=8 m, z_A=5.28 m)
[∂ z(x,y)/∂ r(x,y)](r(x,y)=3·R_m) ≈ -0.02199 m/m (slope - 1.26°, $R_m=R_A$=8 m, z_A=5.28 m)

[∂²z(x,y)/∂[r(x,y)]²](r(x,y)=0·R_m) ≈ -0.0825 1/m (curvature radius -12.12 m, z_A=5.28 m)
[∂²z(x,y)/∂[r(x,y)]²](r(x,y)=1·R_m) = 0 1/m (curvature radius undefined, z_A=5.28 m)
[∂²z(x,y)/∂[r(x,y)]²](r(x,y)=2·R_m) ≈ 0.03349 1/m (curvature radius 29.85 m, z_A=5.28 m)
[∂²z(x,y)/∂[r(x,y)]²](r(x,y)=3·R_m) ≈ 0.00733 1/m (curvature radius 136.37 m, z_A=5.28 m)

.

Regarding that the membrane roof has a roof ridge and so two saddle shaped sides with inclination the overall shape function of each side is given here as

$$z(x,y)=z_m\cdot e^{-\lambda^2[(x-xm)^2+(y-ym)^2]}+c_y\cdot(y-y_0)=z(r(x,y))=z_m\cdot e^{-\lambda^2[r(x,y)^2]}+c_y\cdot(y-y_0)$$

(c_y=5.28 m/26.4 m=0.2, y_0=0 for roof saddle shape side with Gaussian bell curve radial center at (x_A, y_A); c_y=-5.28 m/26.4 m=-0.2, y_0=52.8 m for roof saddle shape side with Gaussian bell curve radial center at (x_B, y_B)).

For the above geometric configuration of the steel cable net the corresponding computational membrane material properties are determined as follows (A in m²/(width in m), A_{Steel} in m²/(width in m)):

$EA=E\cdot 1\text{ m}\cdot d=E_{Steel}\,A_{steel}$
$\nu=\nu_{Steel}$
$\rho_{Steel}(A_{Steel}\cdot 1\text{ m})\cdot 1\text{ m}+\rho_{Steel}(A_{Steel}\cdot 1\text{ m})\cdot 1\text{ m}=\rho\cdot 1\text{ m}\cdot 1\text{ m}\cdot d$
(longitudinal) (orthogonal) (1 m² membrane)

$EA=E\cdot 1\text{ m}\cdot d/(1\text{ m})=E_{Steel}\,A_{steel}$
The computational membrane thickess d is selected here as d=1 cm=0.010 m.
$EA=E\cdot 1\text{ m}\cdot 0.010\text{ m}/(1\text{ m})\approx 2.1e11\text{ N/m}^2\cdot 0.00031415\text{ m}^2/(0.50\text{ m})$
$\underline{E}\approx[2.1e11\text{ N/m}^2\cdot 0.00031415\text{ m}^2/(0.50\text{m})]/[1\text{ m}\cdot 0.010\text{ m}/(1\text{ m})]\approx\underline{1.319e10\text{ N/m}^2}$
$\underline{\nu}=\nu_{Steel}=\underline{0.3}$
$\rho\approx[7860\text{ kg/m}^3\cdot(0.00031415\text{ m}^2/(0.50\text{m})\cdot 1\text{ m})\cdot 1\text{ m}$
$+7860\text{ kg/m}^3\cdot(0.00031415\text{ m}^2/(0.50\text{m})\cdot 1\text{ m})\cdot 1\text{ m}]/[1\text{ m}\cdot 1\text{ m}\cdot d]$
$\underline{\rho}\approx 2\cdot[7860\text{ kg/m}^3\cdot 0.00031415\text{ m}^2/(0.50\text{m})\cdot 1\text{ m}^2]/[1\text{ m}^2\cdot 0.010\text{ m}]\approx\underline{987.7\text{ kg/m}^3}$

Furthermore, for to have a more flexible material for comparative reasons with potentially better convergence behaviour, a second set of computational membrane material properties is applied with E=2.5e9 N/m², ν=0.3, ρ≈987.7 kg/m³.

Gravity is assumed to be 10 m/s² in downward vertical z-direction; so gravity-induced vertical z-displacement is negative.

4.1 Gaussian bell curves (L=88 m, B=52.8 m): Static force equilibrium

For the structural membrane roof with pure Gaussian bell curve shape three cases are considered: Case i) material properties E=2.5e9 N/m², ν=0.3, ρ≈987.7 kg/m³, field displacement [ux=0, uy=0, uz: free] within the inner part of the membrane, excluding rigid edges with boundary conditions [ux=0, uy=0, uz=0], maximum nodal ux-, uy-, or uz-displacement increment is 0.001 m per equilibrium iteration, external load 10 times of its eigenload=10·98.77 N/m²=987.7 N/m², 5700 equilibrium iterations; case ii) material properties E=2.5e9 N/m², ν=0.3, ρ≈987.7 kg/m³, field displacement [ux: free, uy: free, uz: free] within the inner part of the membrane, excluding rigid edges with boundary conditions [ux=0, uy=0, uz=0], maximum nodal ux-, uy-, or uz- displacement increment is 0.001 m per equilibrium iteration, external load 10 times of its eigenload=10·98.77 N/m²=987.7 N/m²,

2000 equilibrium iterations; case iii) material properties E≈1.319e10 N/m², ν=0.3, ρ≈987.7 kg/m³, field displacement [ux=0, uy=0, uz: free] within the inner part of the membrane, excluding rigid edges with boundary conditions [ux=0, uy=0, uz=0], maximum nodal ux-, uy-, or uz- displacement increment is 0.001 m per equilibrium iteration, external load 10 times of its eigenload=10·98.77 N/m²=987.7 N/m², 10000 equilibrium iterations.

Evaluated is the vertical displacement at node 606 (degree of freedom 1818) at x=67.0 m, y=14.0 m, z≈2.777 m, where the curvature of the Gaussian bell curve with maximum vertical elevation of (x_A, y_A, z_A=5.28 m) becomes very small, and at node 777 (degree of freedom 2331) at x=21.0 m, y=38.8 m, z≈2.777 m, where the curvature of the Gaussian bell curve with maximum vertical elevation of (x_B, y_B, z_B=3.28 m) becomes very small. Computational results for case i), ii) and iii) are shown in figure 4.

In figure 4 (very bottom left plot) the position of the two centers of the two Gaussian bell curves (position front right: maximum vertical elevation 5.28 m, position rear left: maximum vertical elevation 3.28 m) within the shape of the roof structure can be located. From figure 4 it can be found that after 5700 equilibrium iterations vertical field displacement [ux=0, uy=0, uz: free] reaches a large maximum value of 0.25 m near the gutter for case i). Case ii) (field displacement [ux: free, uy: free, uz: free]) does not show convergence at all. For case iii) (field displacement [ux=0, uy=0, uz: free]) after 10000 equilibrium iterations vertical field displacement reaches a mamimum value of 0.025 m near the gutter and still is not converged yet. For case iii) after 3950 equilibrium iterations membrane stress evaluation shows maximum tensile stress level of $\sigma_{\xi\xi}^{max,membrane}$=2e6 N/m²=0.2 kN/cm² and $\sigma_{\eta\eta}^{max,membrane}$=3e6 N/m²=0.3 kN/cm² in the two quadrants of the membrane roof structure where the curvature of the two respective Gaussian bell curves is very small; detailed plots of $\sigma_{\xi\xi}^{membrane}$ and $\sigma_{\eta\eta}^{membrane}$ show that around the two Gaussian bell curves tensile stress of lower order of magnitude appears, whereas towards the fixed edges of the membrane roof structure along the gutter (corner regions, where fixed nodes due to zero-displacement boundary conditions hinder the membrane to establish membrane tensile stress state) computational compressive stress appears. It is now mentioned that the computational membrane representation of the steel cable net structure experiences the same strain as the real cable net structure. So steel cable net structure stresses differ from the computational membrane stresses by the factor of $E_{Steel}/E_{computational\ membrane}$. Thus, referring to the above maximum computational membrane stresses of $\sigma_{\xi\xi}^{max,membrane}$=2e6 N/m²=0.2 kN/cm² and $\sigma_{\eta\eta}^{max,membrane}$=3e6 N/m²=0.3 kN/cm², the appropriate maximum steel cable net structure stresses result as $\sigma_{\xi\xi}^{max,steel\ cable\ net}$ $=E_{Steel}/E_{computational\ membrane}\cdot\sigma_{\xi\xi}^{max,membrane}$≈2.100e11/1.319e10·2e6 N/m²≈3.2 kN/cm² and $\sigma_{\eta\eta}^{max,steel\ cable\ net}$ $=E_{Steel}/E_{computational\ membrane}\cdot\sigma_{\eta\eta}^{max,membrane}$≈2.100e11/1.319e10·3e6 N/m²≈4.8 kN/cm² at equilibrium iteration 3950. Vertical displacement is as well the largest in the two quadrants where the curvature of the two Gaussian bell curves is very small. A detailed plot of the vertical displacement shows the vertical displacement around the two Gaussian bell curves. Altogether, considering for case iii) (E≈1.319e10 N/m², ν=0.3, ρ≈987.7 kg/m³, computational membrane representation for steel cable net) the vertical displacement distribution and the equilibrium iteration evolution of the vertical displacement after 10000 iterations (not converged yet) it is concluded that the two Gaussian bell curves within the shape of the roof structure do not deliver sufficient system stiffness throughout the whole roof structure to

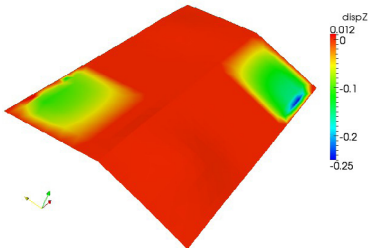

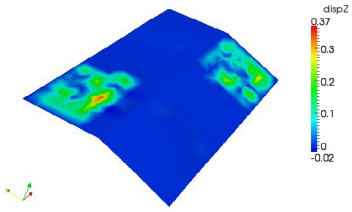

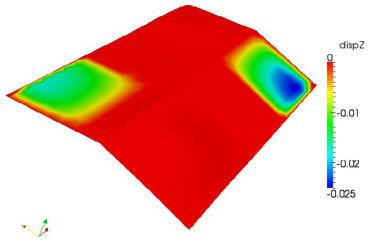

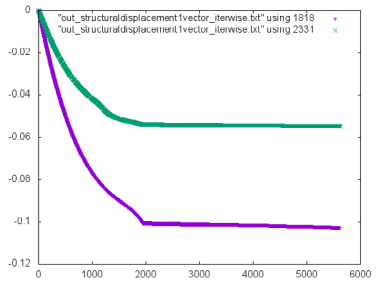

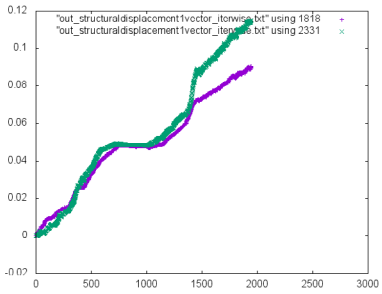

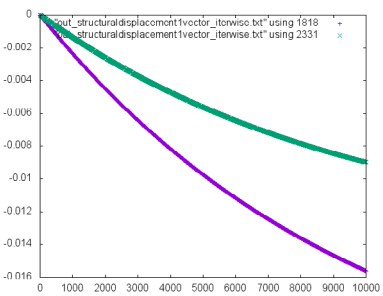

case i) iter 5700 case ii) iter 2000 case iii) iter 10000

case iii) $\sigma_{\xi\xi}^{membrane}$ [N/m²] iter 3950 case iii) $\sigma_{\eta\eta}^{membrane}$ [N/m²] iter 3950 case iii) iter 3950

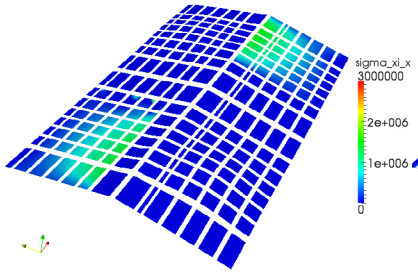

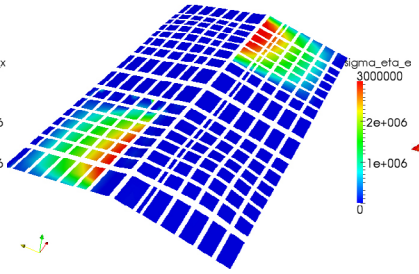

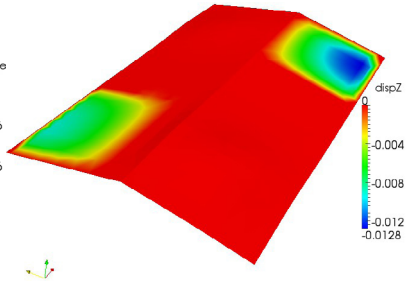

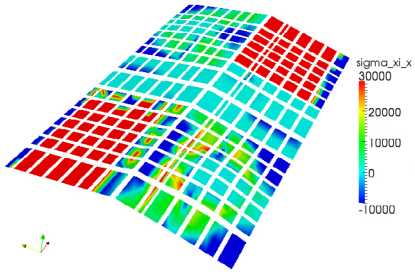

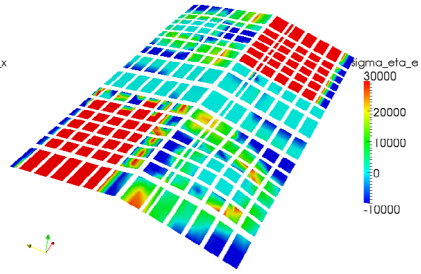

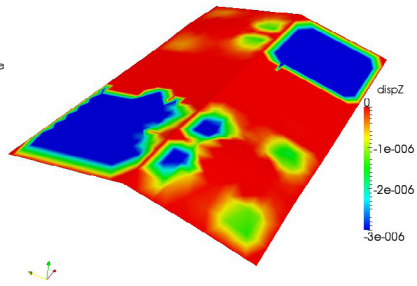

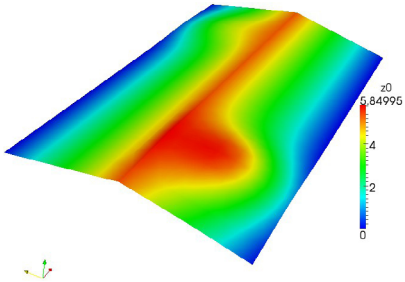

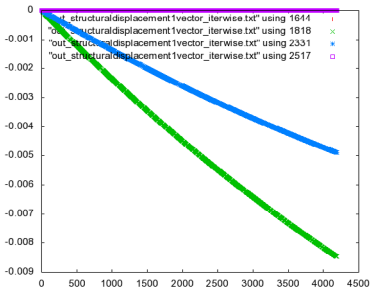

Figure 4: roof structure Gaussian bell curves (L=88 m, B=52.8 m): case i) (top left), case ii) (top center), case iii) (top right) vertical displacement [in m] and membrane nodes 606 and 777 vertical displacement [in m] over cumulated equilibrium iteration index, case iii) (bottom row) membrane stress $\sigma_{\xi\xi}^{membrane}$ [in N/m²] in x-direction and roof structure elevation [in m] (bottom left), membrane stress $\sigma_{\eta\eta}^{membrane}$ [in N/m²] in y-direction (bottom center), vertical displacement [in m] and membrane nodes 606 and 777 vertical displacement [in m] over cumulated equilibrium iteration index (bottom right)

guarantee a limited maximum vertical displacement of the roof structure within an acceptable range of displacement. So, as a consequence, in the two quadrants of the roof structure, where the two Gaussian bell curves have very small curvature, appropriately case a) two Hyparforms of ±1.20 m vertical corner elevation and case b) two Hyparforms of ±0.35 m vertical corner elevation are added to the roof structure shape to give the total shape of the roof structure. The appropriate Hyparforms have their respective centers at (x_C=70.5 m, y_C=13.2 m, z_C=0) and (x_D=17.5 m, y_D=39.6 m, z_D=0).

4.2 Gaussian bell curves and Hypar ±1.20m (L=88m,B=52.8m): Static force equilibrium

For the structural membrane roof with Gaussian bell curve shape and additional Hyparform of ±1.20 m vertical corner elevation four cases are considered:

case i) E=2.5e9 N/m², ν=0.3, ρ≈987.7 kg/m³, field displacement [ux=0, uy=0, uz:free],
case ii) E=2.5e9 N/m², ν=0.3, ρ≈987.7 kg/m³, field displacement [ux:free, uy:free, uz:free],
case iii) E≈1.319e10 N/m², ν=0.3, ρ≈987.7 kg/m³, field displacement [ux=0, uy=0, uz:free],
case iv) E≈1.319e10 N/m², ν=0.3, ρ≈987.7 kg/m³, field displacement[ux:free,uy:free,uz:free].

For all cases i), ii), ii), iv) external load is 10 times the eigenload of the membrane, i.e. 10·98.77 N/m²=987.7 N/m², maximum nodewise ux-, uy- and uz-displacement increment is limited to 0.001 m per equilibrium iteration, 10000 equilibrium iterations are performed. In figure 5 vertical displacement after 10000 equilibrium iterations and the evolution of vertical displacement for node 606 (degree of freedom 1818) and node 777 (degree of freedom 2331) over the cumulated iteration index are shown for case i), ii), iii), iv).

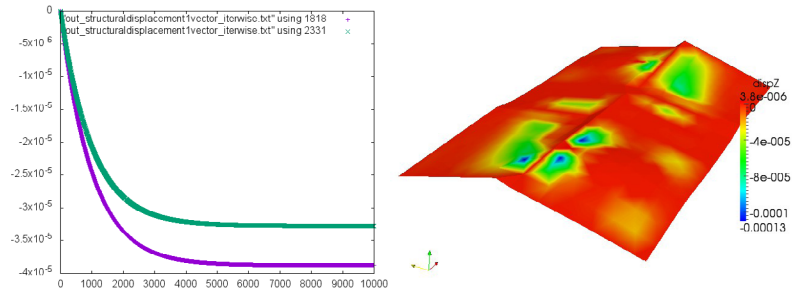

case i)

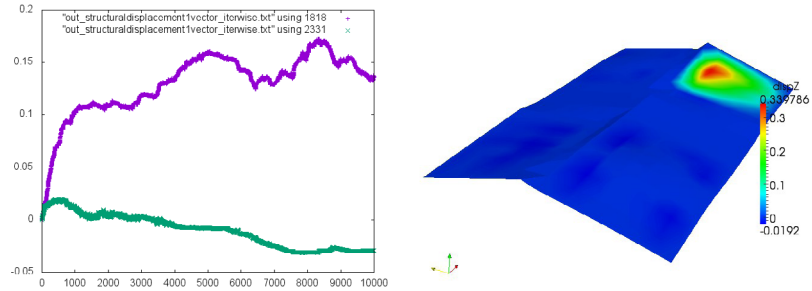

case ii)

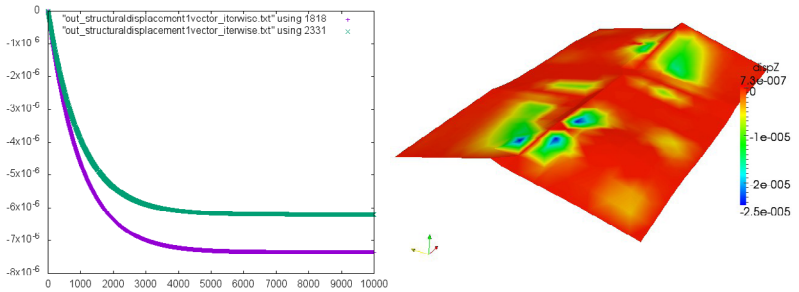

case iii)

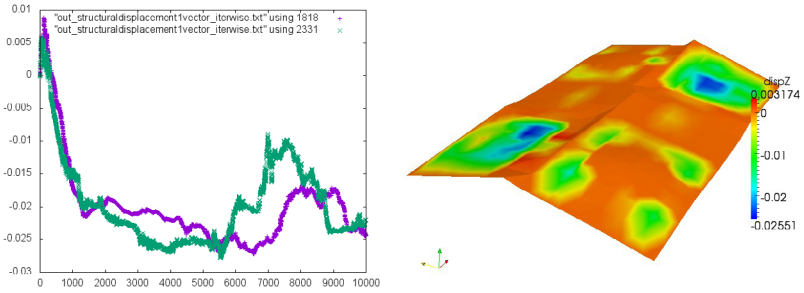

case iv)

Figure 5: roof structure Gaussian bell curves and Hypar ±1.20 m (L=88 m, B=52.8 m): membrane nodes 606 and 777 vertical displacement [in m] over cumulated equilibrium iteration index (left) and vertical displacement [in m] (right) for case i), ii), iii), iv)

Case i) and iii) (both field displacement [ux=0, uy=0, uz: free]) show strictly monotonic evolution in vertical displacement and convergence with very small maximum downward vertical displacement of 0.00013 m (case i)) and 2.5e-5 m (case iii)); the vertical displacement distribution plots indicate the regions of maximum downward vertical displacement. Case ii) (E=2.5e9 N/m², field displacement [ux: free, uy: free, uz: free]) does not show any convergence in vertical displacement after 10000 equilibrium iterations. Case iv) (E≈1.319e10 N/m², field displacement [ux: free, uy: free, uz: free], computational membrane represention of steel cable net) shows continuous evolution with the equilibrium iterations until vertical downward displacement of 0.025 m (node 603, d.o.f 1818) and 0.025 m (node 777, d.o.f. 2331) is reached (approx. eq. iter. 5500), after which a change in vertical displacement appears (approx. eq. iter. 7000) that again leads to a vertical downward displacement of 0.025 m (node 603, d.o.f 1818) and 0.025 m (node 777, d.o.f. 2331) (approx. eq. iter. 10000); so the equilibrium iterations twice lead to the same vertical displacement of 0.025 m (node 603, d.o.f 1818) and 0.025 m (node 777, d.o.f. 2331). The vertical displacement distribution plot indicates the regions of maximum downward displacement (in the two quadrants where the curvature of the two Gaussian bell curves is very small and so the two Hypar shapes are added).

4.3 Gaussian bell curves and Hypar ±0.35m (L=88m,B=52.8m): Static force equilibrium

For the structural membrane roof with Gaussian bell curve shape and additional Hyparform of ±0.35 m vertical corner elevation four cases are considered:

case i) E=2.5e9 N/m², ν=0.3, ρ≈987.7 kg/m³, field displacement [ux=0, uy=0, uz:free],
case ii) E=2.5e9 N/m², ν=0.3, ρ≈987.7 kg/m³, field displacement [ux:free, uy:free, uz:free],
case iii) E≈1.319e10 N/m², ν=0.3, ρ≈987.7 kg/m³, field displacement [ux=0, uy=0, uz:free],
case iv) E≈1.319e10 N/m², ν=0.3, ρ≈987.7 kg/m³, field displacement[ux:free,uy:free,uz:free].

For all cases i), ii), ii), iv) external load is 10 times the eigenload of the membrane, i.e. 10·98.77 N/m²=987.7 N/m², maximum nodewise ux-, uy- and uz-displacement increment is limited to 0.001 m per equilibrium iteration, 10000 equilibrium iterations are performed. In figure 6 vertical displacement after 10000 equilibrium iterations and the evolution of vertical displacement for node 606 (degree of freedom 1818) and node 777 (degree of freedom 2331) over the cumulated iteration index are shown for case i), ii), iii), iv).

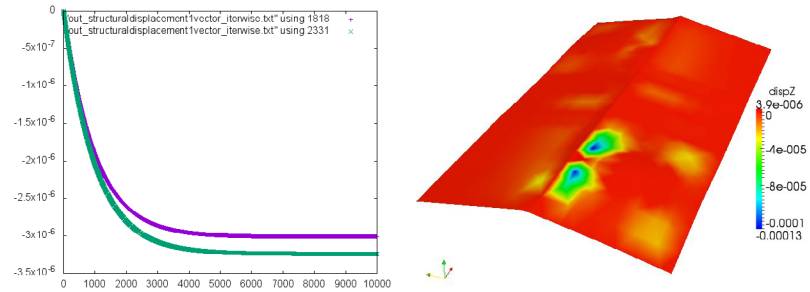

case i)

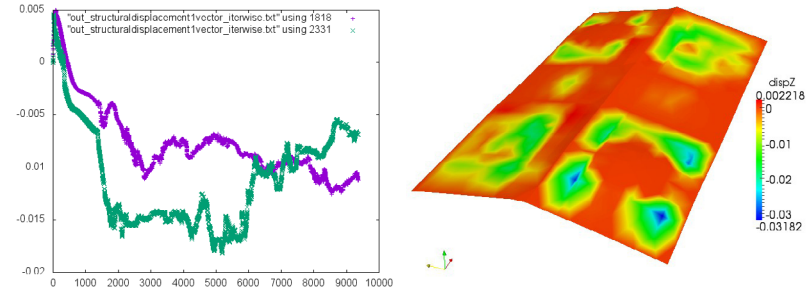

case ii)

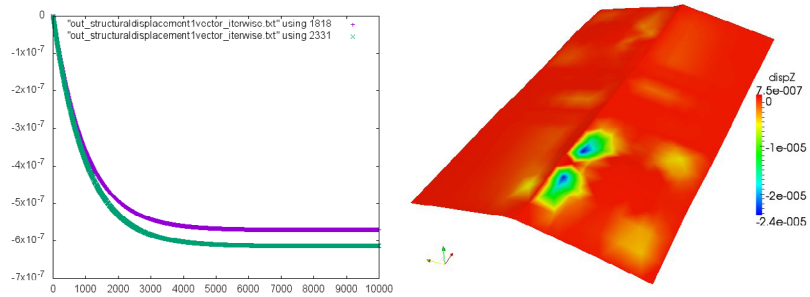

case iii)

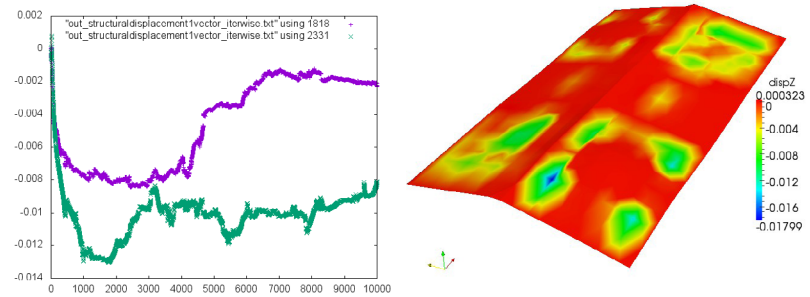

case iv)

Figure 6: roof structure Gaussian bell curves and Hypar ±0.35 m (L=88 m, B=52.8 m): membrane nodes 606 and 777 vertical displacement [in m] over cumulated equilibrium iteration index (left) and vertical displacement [in m] (right) for case i), ii), iii), iv)

Case i) and iii) (both field displacement [ux=0, uy=0, uz: free]) show strictly monotonic evolution in vertical displacement and convergence with very small maximum downward vertical displacement of 0.00013 m (case i)) and 2.4e-5 m (case iii)); the vertical displacement distribution plots indicate the regions of maximum downward vertical displacement (maximum vertical downward displacement for case i) and iii) has the same order of magnitude as for case i) and iii) with Gaussian bell curves and Hypar ±1.20 m (see above)). Case ii) (E=2.5e9 N/m², field displacement [ux: free, uy: free, uz: free]) shows a constant range for vertical downward displacement of node 603 (d.o.f. 1818) around 0.01 m (eq. iter. 3000 to 10000), whereas for node 777 (d.o.f. 2331) vertical downward displacement reaches a constant range of 0.015 m (eq. iter. 2000 to 6000) and then experiences a change to around 0.01 m (eq. iter. 6500 to 10000); the vertical displacement distribution plot indicates the regions of maximum downward vertical displacement of 0.032 m. Case iv) (E≈1.319e10 N/m², field displacement [ux: free, uy: free, uz: free], computational membrane represention of steel cable net) shows a constant range of vertical displacement for node 777 (d.o.f. 2331) around 0.01 m, whereas for node 603 (d.o.f. 1818) vertical downward displacement reaches 0.008 m (eq. iter. 1000 to 4500) and then changes to a constant range around 0.002 m (eq. iter. 6500 to 10000); the vertical displacement distribution plot indicates the regions of maximum downward vertical displacement of 0.018 m. Altogether displacement distributions due to external load (10 times of the membrane´s eigenload=10·98.77 N/m²=987.7 N/m²) onto the membrane show representative displacement distributions for cases ii) and iv) (both field displacement [ux: free, uy: free, uz: free]) and also acceptable maximum downward displacement of 0.032 m (case ii), E=2.5e9 N/m²) and particularly 0.018 m (case iv), E≈1.319e10 N/m², computational membrane representation of steel cable net) with the roof structure of two Gaussian bell curves and additional two Hypar ±0.35 m. Thus the structural roof shape that is designed with two Gaussian bell curves and additional two Hypar ±0.35 m is assessed as favourable to be selected as a structural roof shape of sufficient system stiffness against external vertical downward load in the range of 1 kN/m².

4.4 Gaussian bell curves and Hypar ±0.35m (L=88 m, B=52.8 m): Exposure to eigenload

For the analyzed-above structural membrane roof with Gaussian bell curve shape and additional Hyparform of ±0.35 m vertical corner elevation the case

E≈1.319e10 N/m², ν=0.3, ρ≈987.7 kg/m³, field displacement [ux:free,uy:free,uz:free]

is considered for vertical eigenload of the membrane, i.e. 98.77 N/m² (distributed eigenmass of the steel cable net and so its computational membrane representation is 987.7 kg/m³·0.01 m=9.877 kg/m²≈10 kg/m²). This case represents the considered steel cable net when potentially in addition dynamic load e.g. due to wind (uprising forces) might appear. Maximum nodewise ux-, uy- and uz-displacement increment is limited to 0.001 m per equilibrium iteration, 10000 equilibrium iterations are performed. In figure 7 vertical displacement after 10000 equilibrium iterations and the evolution of vertical displacement as well as horizontal displacement for node 606 (degree of freedom 1818) and node 777 (degree of freedom 2331) over the cumulated iteration index are shown.

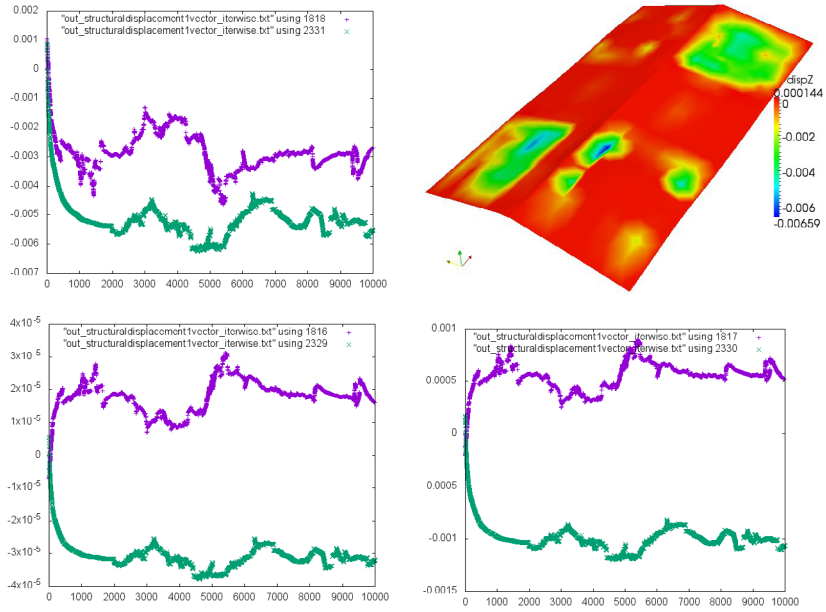

Figure 7: roof structure Gaussian bell curves and Hypar ±0.35 m (L=88 m, B=52.8 m): membrane nodes 606 and 777 vertical displacement [in m] over cumulated equilibrium iteration index (top left) and vertical displacement [in m] (top right) for exposure to eigenload (98.77 N/m²), membrane node 606 and 777 horizontal x-displacement [in m] (bottom left) and horizontal y-displacement [in m] (bottom right) over cumulated equilibrium iteration index

The equilibrium iteration evolution shows a range of vertical downward displacement of 0.003 m for node 603 (d.o.f. 1818) (eq. iter. 1500 to 10000 with an intermediate variation from eq. iter. 3000 to 5500) and 0.005 m for node 777 (d.o.f. 2331) (eq. iter. 1000 to 10000). The vertical displacement distribution plot indicates the region with maximum downward vertical displacement of 0.0066 m≈0.007 m. Horizontal x-displacement reaches a range of +2e-5 m (node 603, d.o.f. 1816) and -3e-5 m (node 777, d.o.f. 2329), horizontal y-displacement reaches a range of +0.0005 m (node 603, d.o.f. 1817) and -0.001 m (node 777, d.o.f. 2330).

4.5 Gaussian bell curves and Hypar ±0.35m (L=88m,B=52.8m):Surround.visc.fluid flow

The computational membrane roof structure with two Gaussian bell curves and additional Hypar ±0.35m (L=88 m, B=52.8 m) with its museum building underneath is surrounded by viscous fluid flow (eventually to model transient air flow along the elastic structural membrane roof structure). Therefore the surrounding viscous fluid flow is modeled by the Navier-Stokes equations for laminar viscous fluid flow. The computational fluid domain stretches horizontally from x=-176 m to x=264 m and from y=-105.6 m to y=158.4 m and stretches vertically from -8 m to 10 m, where at the center of the fluid domain with dimensions of the museum domain a void is located within the fluid domain. Flow direction is case a) considered in horizontal x-direction and case b) considered in horizontal y-direction. For both case a) and case b) the fluid domain is discretized with 8-node hexahedra elements

with linear interpolation functions. For both case a) and case b) the fluid domain is horizontally discretized with 30 element layers upstream of the museum structure, with 30 element layers along the museum structure and with 30 element layers downstream of the museum structure all in flow direction and is horizontally discretized with 10 element layers left of the museum structure, with 30 element layers along the museum structure and with 10 element layers right of the museum structure all transversal to the flow direction. In vertical direction the fluid domain is discretized with altogether 36 element layers, 14 of which are located from soil to below bottom of the roof structure, 14 of which are located from below bottom of the roof structure to above top of the roof structure and 8 of which are located from above top of the roof structure to about 5 m above top of the roof structure. Fluid elements´ edge lengths range from 0.5 m to a few meters. In the vicinity of the museum structure fluid element lengths are about 0.5 m. As the regions directly upstream and directly downstream of the museum structure are discretized with higher refinement of the mesh than the regions laterally left and right of the museum structure for case a) (flow in x-direction) and case b) (flow in y-direction) two different fluid meshes, but both with the same number of fluid nodes and same number of fluid elements, namely 159943 fluid nodes and 149400 fluid elements, are used. The two different computational fluid domains for case a) (flow in x-direction) and case b) (flow in y-direction) are illustrated in figure 8. The fluid mesh discretization is nonsymmetric.

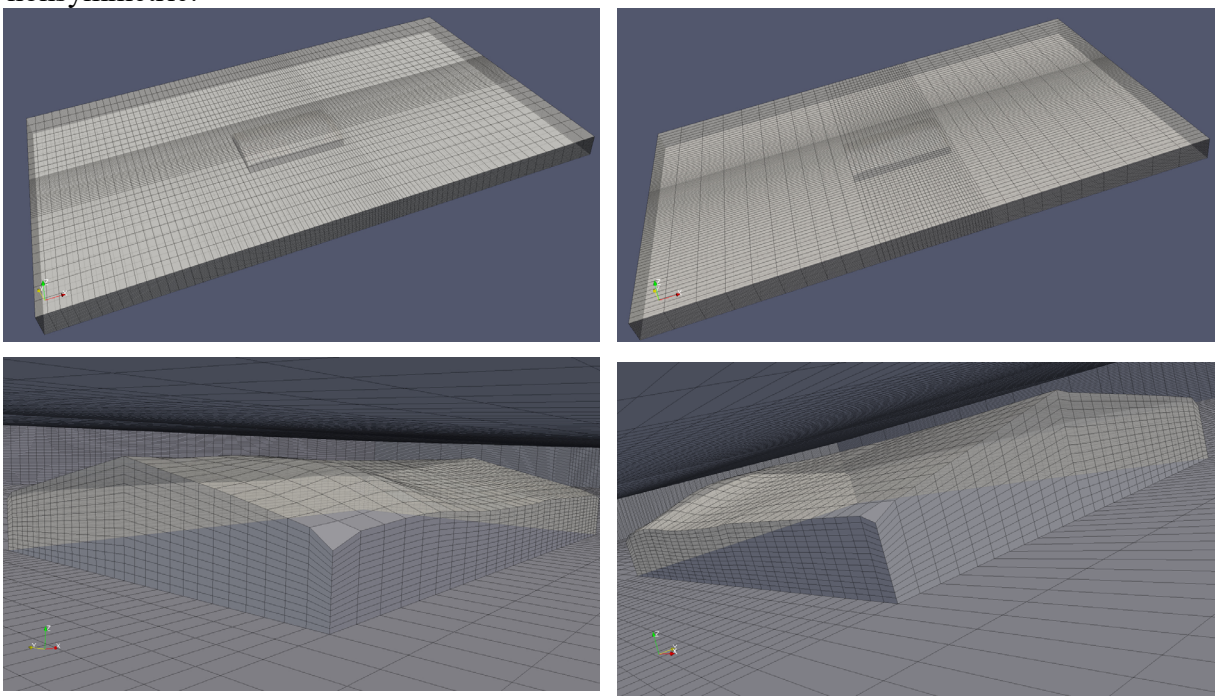

Figure 8: computational fluid domain for flow in x-direction (left), flow in y-direction (right)

At the beginning of computations for case a) and case b) the fluid within the computational fluid domain is completely at rest, i.e fluid velocity vector and fluid pressure are completely zero throughout the whole fluid domain. Boundary conditions define zero normal velocity at left, right, bottom and top boundary of the fluid domain. On the upstream boundary, inflow

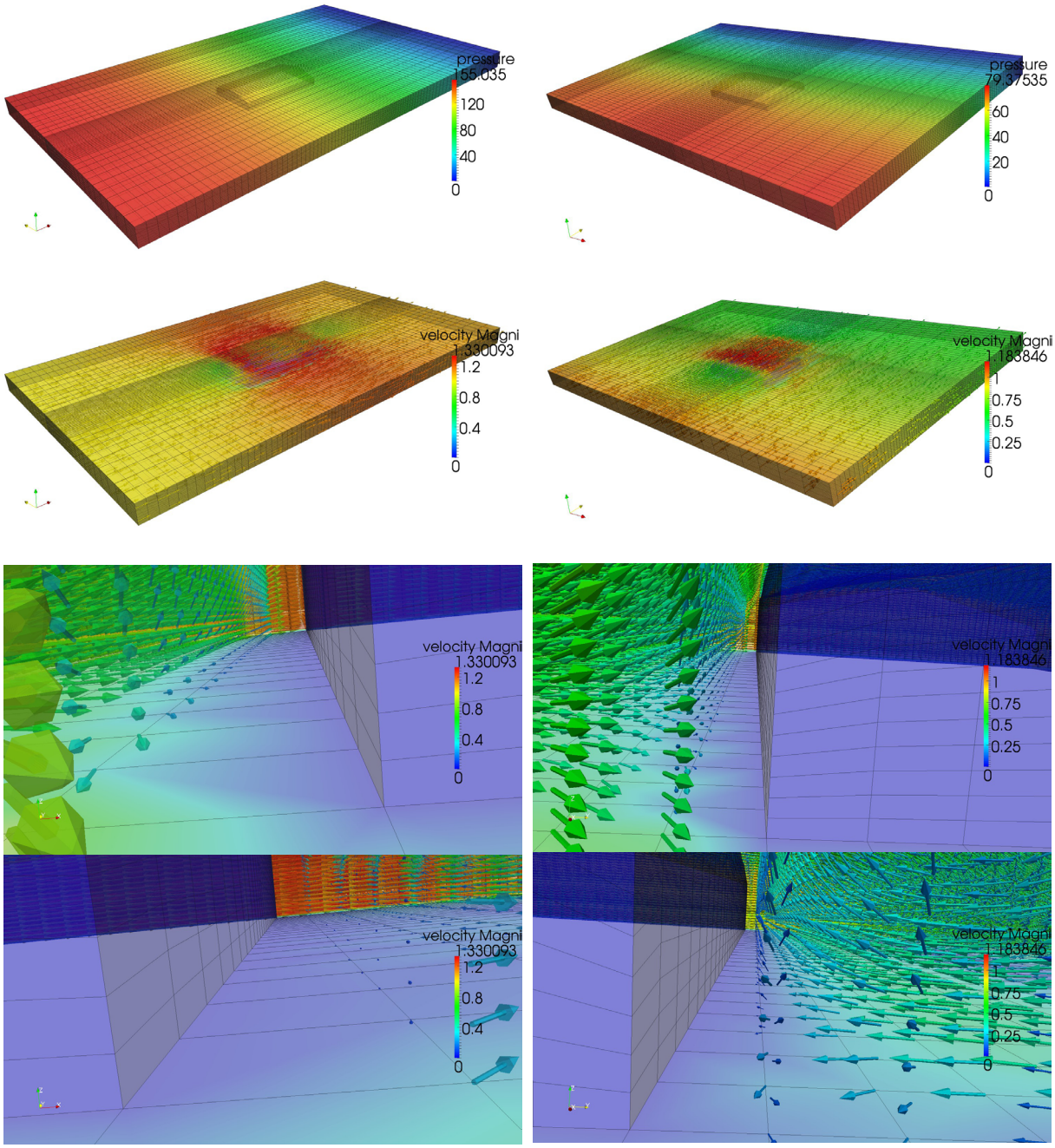

case a) (flow in x-direction at t=38.7 s) case b) (flow in y-direction at t=23.6 s)

Figure 9: fluid state for case a) flow in x-direction (left) and case b) flow in y-direction (right): fluid pressure field (top), fluid velocity field (second top), fluid velocity upstream of structure (second bottom) with upward velocity direction, fluid velocity downstream of structure (bottom) with reversing upstream velocity direction near bottom within vortex downstream of structure

velocity of 1.0 m/s is defined. On the downstream boundary, outflow pressure of zero is defined. On all boundaries of the structural museum domain, i.e. upstream and downstream museum surface and left and right lateral museum surface and top museum roof surface (with two Gaussian bell curves and additional two Hypar ±0.35m), fluid velocity vector is defined as the zero vector. Time domain computations are performed with 0.1 s constant time interval size and 3 equilibrium iterations within the fluid equation solution scheme for each considered time interval. Fluid material properties are (dynamic) viscosity μ_F=0.5 kg/(m·s) and density ρ_F=1.0 kg/m³. Time integration is performed for case a) as well as for case b) using a constant time interval size of 0.1 s for a total of 400 time intervals. Fluid pressure distribution and fluid velocity distribution for case a) timestep 387 (38.7 s) and for case b) timestep 263 (26.3 s) are shown in figure 9.
Figure 9 shows the fluid pressure field where upstream pressure is high and downstream pressure is zero at the outflow boundary. The fluid velocity field shows higher velocity magnitude above the structure. At the upstream end of the museum structure the velocity field is directed vertically upward, at the downstream end of the museum structure an at the bottom upstream directed vortex flow is found.

5 CONCLUSIONS

Membrane roof structures of continuously opposite curvature (so-called negative curvature) are considered. Structural membrane force equilibrium due to static and dynamic external load without pretension of the membrane is obtained by a constant range of displacement after about 100 to 1000 to 10000 equilibrium iterations where nodewise componentwise displacement increment is limited to between 0.01 m and 0.0001 m per equilibrium iteration. Boundary conditions that fix the horizontal movement of membrane field finite element nodes to reduce the number of degrees of freedom lead to very small vertical membrane displacement. In contrast, boundary conditions that allow completely free horizontal as well as vertical displacement for membrane nodes apart from boundary edges lead to finite vertical displacement of a few centimeters that reaches the order of approximately 1/100 and 1/300 of the respective span-width of the membrane roof, which seems acceptable for the considered steel cable net structures that are computationally represented by membrane roof structures, here a Hyparform (L=5 m) and a museum building with saddle shaped roof structure (L=88 m, B=52.8 m) with two Gaussian bell curves (and additional Hypar), for the latter of which analytic assessment of curvature distribution is taken into account. The distributed eigenmass of the roof structures is of order 10 kg/m². Surrounding viscous fluid flow around the considered museum structure shows typical vortex patterns in the leeward zone downstream of the museum building (obstacle) within the fluid domain. A strongly coupled segregated approach for fluid-structure interaction between structural membranes and viscous (laminar) fluid flow is presented together with an altogether (nonlinear) interpolation procedure to interpolate viscous fluid load onto the membrane structure and to interpolate structural membrane load onto the adjacent viscous fluid for pairs of non-matching structural membrane mesh and viscous fluid meshes.

REFERENCES

[1] H. Apelmann, C. Gengnagel. Interaktion von Membranen und biegesteifen Bogentragwerken. Stahlbau 72, Heft 10, 702-707, 2003

[2] K.-J. Bathe. Finite-Elemente-Methoden. Springer-Verlag Berlin, 2002

[3] H. Berger. Light structures – structures of light. Birkhäuser, Basel/Boston/Berlin, 1996

[4] K.-U. Bletzinger. Formfindung von leichten Tragwerken. in Baustatik-Baupraxis (Hrsg. D. Dinkler), 99-110, Institut für Statik, Technische Universität Braunschweig, 2002

[5] K.-U. Bletzinger, E. Ramm. Structural optimization and form finding of light weight structures. Computers and Structures 79, 2053-2962, 2001

[6] K.-U. Bletzinger, R. Ziegler. Theoretische Grundlagen der numerischen Formfindung von Membrantragwerken und Minimalflächen. Beton-Kalender BK2, 2000, 441-456, Ernst & Sohn, Berlin, 2000

[7] G. Brinkmann (Hrsg.). Weitgespannte Flächentragwerke. Zusammenfassender Bericht, SFB 64, Universität Stuttgart, 1990

[8] A. Brooks and T.J.R. Hughes. Streamline upwind/Petrov-Galerkin formulations for convection dominated flows with particular emphasis on the incompressible Navier-Stokes equations, Computer methods in applied mechanics and engineering, 32, 199-259, 1982.

[9] E. Bubner et al. Minimalkonstruktionen. Symposium Universität Essen Gesamthochschule, 1977

[10] E. Bubner et al. Membrankonstruktionen, Teil 1, Teil 2, Teil 3, Teil 4. Haus der Technik Essen / Universität Essen Gesamthochschule, 1979-1982

[11] H. Bufler. Pressure loaded structures under large deformations. Zeitschrift für Angewandte Mathematik und Mechanik 64, Heft 7, 287-295, 1984

[12] C. Corte, J. Garcia, E. Oñate. Three-dimensional flow around rigid and elastic cylindrical structures. 32 pages, CIMNE Barcelona, 2007

[13] C. Corte, J. Garcia, E. Oñate. A strongly-coupled segregated approach for finite element modeling of fluid-structure interaction. 17 pages, CIMNE Barcelona, 2008

[14] C. Corte. A segregated approach for strong coupling of finite element solvers to model fluid-structure interaction. 30 pages, CIMNE Barcelona, 2008

[15] C. Corte. A 3D approach for finite element modeling of viscous fluid flow. 24 pages, Dr. C. Corte, Baustatik – Baudynamik – Numerische Modellierung, Berlin, Tel./Fax +49(0)30-347871 78/80, 2010

[16] C. Corte. A 3D approach for finite element modeling of fluid-structure interaction between incompressible viscous fluids and elastic structures. 64 pages, Dr. C. Corte, Baustatik – Baudynamik – Numerische Modellierung, Berlin, Tel./Fax +49-(0)30-347871 78/80, 2011

[17] C. Corte. Finite element modeling of fluid-structure interaction for an elastic 2D flag in harmonic viscous fluid flow and an elastic 3D sail structure in stationary viscous fluid flow. 39 pages, Dr. C. Corte, Baustatik – Baudynamik – Numerische Modellierung, Berlin, Tel./Fax +49-(0)30-347871 78/80, 2012

[18] C. Corte. 3D-Membrantheorie. Stahlbau 83, Heft 5, 343-358, Ernst und Sohn Verlag, 2014.

[19] C. Corte. 3D membrane theory. 11th World Congress on Computational Mechanics, 268-292, Barcelona/Spain, 2014
[20] J. Cremers, G. Grunwald. Innovative Membran-Stadiondächer in Kiew, Warschau und Vancouver. Stahlbau 80, Heft 9, 678-686, 2011
[21] H. Dirlewanger et al. Ausgewählte Flächentragwerke. Internationales Symposium Weitgespannte Flächentragwerke, SFB 64, Universität Stuttgart, 1976
[22] P. Drew. Tensile structures. Granada publishing London, 1979
[23] P. Drew. New tent architecture. Thames and Hudson, 2007
[24] O. Frei, Das hängende Dach, Technische Universität Berlin, 1954
[25] O. Frei et al. Mitteilungen der Entwicklungsstelle für den Leichtbau in Berlin. Nr. 7, Nr. 8, Nr. 9. Entwicklungsstelle für den Leichtbau in Berlin, 1961-1963
[26] O. Frei, R. Trostel. Zugbeanspruchte Konstruktionen, Band 1. Ullstein Fachverlag Berlin/Frankfurt, 1962
[27] O. Frei, F.-K. Schleyer. Zugbeanspruchte Konstruktionen, Band 2. Ullstein Fachverlag Berlin/Frankfurt, 1966
[28] K. Göppert. Membrankonstruktionen – Form und Detail. Stahlbau 73, Heft 12, 990-1000, 2004
[29] H. M. Hilber, T. J. R. Hughes, R. L. Taylor. Improved numerical dissipation for time integration algorithms in structural dynamics. Earthquake engineering and structural dynamics, vol. 5, 283-292, 1977
[30] D. Hoppe. Textile Membrankonstruktionen. Böhlau Verlag Wien/Köln/Weimar, 2007
[31] J. Linhard. Numerisch-mechanische Betrachtung des Entwurfsprozesses von Membrantragwerken. TU München, 2009
[32] K. Linkwitz, H.-J. Schek. Einige Bemerkungen zur Berechnung von vorgespannten Seilnetzkonstruktionen. Ingenieur-Archiv 40, 145-158, 1971
[33] S. Neuhäuser et al. Adaptive Tragwerke – Aktuelle Forschung im Ultraleichtbau. Stahlbau 82, Heft 6, 428-437, 2013
[34] W. Renner. Membrantragwerke – Konzepte, Bemessung, Ausführung. Stahlbau 69, Heft 7, 2000
[35] C. Roland. Frei Otto – Spannweiten. Ullstein Fachverlag Berlin/Frankfurt, 1965
[36] H.-J. Schock. Segel, Folien und Membranen. Birkhäuser, Basel/Boston/Berlin, 1997
[37] M. Seel, G. Siebert. Analytische Lösungen für Kreis- und Kreisringplatten unter symmetrischer und antimetrischer Einwirkung. Stahlbau 81, Heft 9, 711-718, 2012
[38] Weitgespannte Flächentragwerke, Band 1 bis 3. Internationales Symposium Weitgespannte Flächentragwerke, SFB 64, Universität Stuttgart, 1976
[39] Weitgespannte Flächentragwerke. Band 1 und 2. 2. Internationales Symposium Weitgespannte Flächentragwerke, SFB 64, Universität Stuttgart, 1979
[40] R. Wüchner, K.-U. Bletzinger. Stress-adapted numerical form finding of pre-stressed surfaces by updated reference strategy. International Journal for Numerical Methods in Engineering 64, 143-166, 2005
[41] R. Wüchner. Mechanik und Numerik der Formfindung und Fluid-Struktur-Interaktion von Membrantragwerken. TU München, 2006
[42] J. Zerning. Design guide to anticlastic structures in plastic. Polytec of London, 1975